

Automated Liver Vein Segmentation in Pre- operative Roadmapping Using Non-Contrast MRI

BSc Thesis

J.C.J. Sallevelt

Committee:

Dr. Ir. W.M. Brink

MSc E. Ilia

Ir. J.L. van der Hoek

June 22, 2025

Biomedical Engineering

Faculty Science and Technology

UNIVERSITY OF TWENTE. | TECHMED CENTRE

Abstract

Background: Budd-Chiari Syndrome (BCS) is a rare hepatic vascular disorder characterised by obstruction of hepatic venous outflow. Detailed venous imaging is crucial for preoperative planning. Current imaging techniques often rely on ionising radiation combined with iodine contrast medium, posing health risks to patients. Magnetic Resonance Angiography (MRA) is typically performed using gadolinium-based contrast agents, which also carry potential risks. This study investigates whether a deep learning model can accurately segment the hepatic veins on non-contrast MRI using a balanced Steady-State Free Precession (b-SSFP) sequence.

Methods: An nnU-Net v2 model was trained on 23 annotated datasets acquired at Radboud University Medical Center (Nijmegen, Netherlands) using a 3 Tesla MRI scanner. Model validation was performed on data from four healthy volunteers scanned with a 1.5T MRI at the University of Twente (Enschede, Netherlands). Quantitative analysis was performed by calculating an average Dice score, sensitivity, and specificity. For qualitative analysis, a 3D reconstruction was created for visual assessment. Additionally, a 3D-printed silicone liver phantom with hollow veins was developed, and a catheter-based intervention was simulated as an in-vitro experiment to assess clinical applicability.

Results: The model achieved an average Dice score of 0.88, sensitivity of 0.85 and a specificity of 1.00 on the independent validation set. Visual analysis showed accurate segmentation of the major hepatic veins. Discrepancies between AI- and manual segmentation were found in smaller peripheral branches, which can be filtered out through post-processing.

Conclusion: The trained model can accurately segment veins on non-contrast MRI. This technique has potential for clinical implementation in preoperative roadmapping and, in the future, intraoperative guidance, offering a safer alternative to contrast-enhanced imaging.

Contents

1	List of Abbreviations	3
2	Introduction	4
3	Methods	6
3.1	MRI Acquisition Protocol	6
3.2	Manual Data Segmentation	6
3.3	AI Model Development	7
3.4	Quantitative Validation	7
3.5	Qualitative Validation	8
3.6	In-Vitro Assessment	8
4	Results	9
4.1	Model Training	9
4.2	Model Validation	10
4.3	Postprocessing	10
4.4	Phantom Intervention	13
5	Discussion	14
5.1	Clinical Implications	14
5.2	Study Limitations	15
5.3	Recommendation	16
6	Conclusion	17
7	Acknowledgments	18

1 List of Abbreviations

Abbreviation	Meaning
3D	Three-Dimensional
AI	Artificial Intelligence
BCS	Budd-Chiari Syndrome
b-SSFP	Balanced Steady-State Free Precession
CT	Computed Tomography
CNN	Convolutional Neural Network
EMA	European Medicines Agency
FA	Flip Angle
FDM	Fused Deposition Modeling
FOV	Field of View
GBCAs	Gadolinium-Based Contrast Agents
HV	Hepatic Veins
ICM	Iodine Contrast Medium
IVC	Inferior Vena Cava
MR	Magnetic Resonance
MRA	Magnetic Resonance Angiography
MRI	Magnetic Resonance Imaging
MRV	Magnetic Resonance Venography
NSF	Nephrogenic Systemic Fibrosis
PE	Phase Encoding
PAT	Parallel Acquisition Technique
PVA	Polyvinyl Alcohol
Radboud UMC	Radboud University Medical Center
SNR	Signal-to-Noise Ratio
TA	Time of Acquisition
TE	Echo Time
TR	Repetition Time
UTwente	University of Twente
VIBE	Volumetric Interpolated Breath-hold Examination

2 Introduction

Budd-Chiari Syndrome (BCS) is a rare, potentially life-threatening hepatic vascular disorder characterised by complete blockage or stenosis of the hepatic venous outflow tract [1, 2]. BCS can be divided into two categories: primary BCS and secondary BCS [3]. Secondary BCS is caused by external compression or invasion of the hepatic veins or inferior vena cava, often due to conditions such as cysts, malignancies, or abscesses. In contrast, primary BCS results from intraluminal narrowing, typically caused by phlebitis or thrombosis [4]. This paper will focus on endovascular interventions via the venous system, where primary BCS is the most relevant clinical condition. Therefore, in the remainder of the report, the term BCS will refer specifically to primary Budd-Chiari Syndrome.

Thrombosis is the primary cause of BCS, which has been diagnosed in approximately 1 in 100,000 individuals [1, 6]. A thrombus can cause a partial or complete obstruction in the small hepatic veins, large hepatic veins (HV), the inferior vena cava (IVC), or a combination of these vessels (see Figure 1) [2, 3]. In western countries, obstruction of the hepatic veins is the most commonly observed condition. Obstruction of the hepatic veins leads to postsinusoidal portal hypertension, resulting in a reduction of portal venous inflow. In the absence of intervention, this hemodynamic disturbance causes fluid accumulation within the liver (hepatic congestion) and the peritoneal cavity (ascites) [1]. The reduction in venous outflow creates a hypoxic environment within the liver, ultimately leading to hepatocellular necrosis [6]. If the extent of necrosis is severe, this can result in acute liver failure, a fatal condition. Over a longer period of time – typically within a few weeks after the obstruction – this process may evolve into hepatic fibrosis, eventually progressing to liver cirrhosis. In general, if left untreated, Budd-Chiari Syndrome is a progressive and fatal disease.

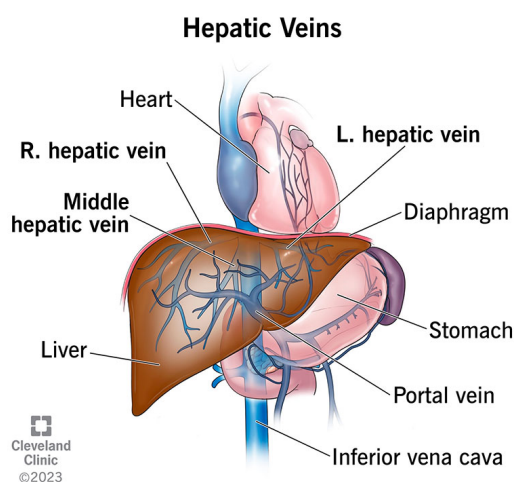


Figure 1: Anatomical illustration of the hepatic venous system. The portal vein is an afferent vessel that transports blood from the gastrointestinal system to the liver. The right, middle, and left hepatic veins are efferent vessels that carry deoxygenated blood from the liver to the inferior vena cava, from where the blood returns to the heart [5].

After diagnosis of BCS has been established, a treatment plan must be formulated to restore hepatic vein outflow [7]. The chosen therapeutic approach is determined in a multidisciplinary team, taking into account factors such as the underlying cause and the severity of the condition. If anticoagulant therapy proves insufficient, an endovascular intervention may be performed by an interventional radiologist. Among patients with BCS, 50-80% undergo an endovascular intervention, with angioplasty alone being sufficient in 13-49% of these cases [8-10]. In the remaining group of patients, a stent was also placed, which has been shown to reduce the risk of reobstruction [11, 12]. Before the vascular intervention takes place, medical imaging is important to map the anatomical structure of the hepatic veins [11, 13].

Current imaging techniques used during endovascular interventions – such as 3D fluoroscopy and CT (computed Tomography)[14] – pose significant health risks. These methods rely on ionising radiation combined with iodine contrast medium (ICM). Cumulative radiation exposure exceeding 100 mGy has been linked to an increased risk of malignancies [15]. In CT fluoroscopy,

patients may be exposed to total doses exceeding this threshold depending on procedure duration [16]. Operators are also affected, receiving up to 1.1 mGy/sec to their hands. Additionally, ICM can cause adverse effects, ranging from mild nausea to severe reactions such as cardiac arrest [17].

Magnetic Resonance Angiography (MRA) can be utilised to visualise hepatic vasculature without ionising radiation, but this typically requires the intravenous administration of gadolinium-based contrast agents (GBCAs), such as gadobutrol or gadobenic acid [18, 19]. While GBCAs are generally considered safe, they are not without risk. Adverse reactions – though rare – can include anaphylactic shock and nephrogenic system fibrosis (NSF), particularly in patients with impaired renal function [20, 21]. Additionally, GBCAs can be nephrotoxic at high concentrations and it is therefore recommended to avoid administering a second dose of GBCA within 48 hours to prevent kidney damage [22].

Considering the aforementioned risks – radiation exposure, ICM reactions, and GBCA toxicity – this study explores the use of non-contrast MRI as a safer alternative. Recent advances in artificial intelligence (AI), particularly in deep learning medical segmentation, offer promising alternatives for reducing the use of GBCAs [23]. Recent studies have demonstrated that a convolutional neural network (CNN) can post-process MRI images to enhance contrast, enabling a reduction of GBCA dose by 90% [24–26]. However, these studies also indicate that excluding GBCAs entirely leads to insufficient image contrast, limiting the performance of AI algorithms compared to full-dose Gd administration. Besides AI-based contrast enhancement, the choice of MRI acquisition protocol plays a critical role in vascular visualisation without contrast agents. For instance, 4D flow MRI can be used to visualise abdominal veins by identifying peak blood flow exceeding a certain threshold value, which serves as an indicator of vascular lumen [27]. Additionally, AI models have successfully segmented liver veins on a non-contrast T₁-weighted Dixon sequence [28]. However, balanced steady-state free precession (b-SSFP) is a technique known for generating a high signal-to-noise ratio (SNR) and vascular contrast [29]. Furthermore, the nnU-Net framework – specifically the enhanced version, nnU-Net v2 – has thus far well performed across a wide range of medical imaging tasks, with minimal manual tuning required [30]. Therefore, this study investigates the use of a b-SSFP sequence combined with the nnU-Net v2 framework for liver vein segmentation, aiming to improve the interventional workflow and expand treatment accessibility for patients who are known to react poorly to gadolinium-based contrast agents.

Given the clinical importance of pre-interventional hepatic vein mapping and the risks associated with gadolinium-based contrast agents, this study investigates whether artificial intelligence can be used for segmentation on non-contrast MRI. The following research question will be addressed: Can a deep learning model, trained on annotated non-contrast MRI data, accurately perform automatic segmentation of hepatic veins on non-contrast MRI?

It is expected that this model could generate an accurate high-quality, non-contrast anatomical roadmap [28] that can aid interventional radiologists in planning and performing endovascular interventions for Budd-Chiari syndrome.

3 Methods

Prior to this study, 23 liver MRI datasets were obtained in healthy volunteers (age range: 23–80 years) at Radboud University Medical Center (Radboud UMC) in Nijmegen, Netherlands. Manual segmentation of the hepatic veins, including the vena cava and portal vein, was performed to serve as ground truth for the AI model training. The model was subsequently validated using MRI data from four additional subjects. Finally, a 3D liver model was printed and used in a simulated endovascular intervention to evaluate clinical applicability.

3.1 MRI Acquisition Protocol

MRI scans at Radboud UMC were obtained using a balanced steady-state free precession (b-SSFP) sequence on a 3 Tesla MRI scanner. For validation, four healthy volunteers were scanned at the University of Twente (UTwente) TechMed Centre using a 1.5 Tesla MRI scanner. During data acquisition, participants were instructed to hold their breath for approximately twenty seconds to reduce respiratory motion artifacts. To ensure consistency and comparability, a similar b-SSFP protocol was used. An overview of the protocols is provided in Table 1. The b-SSFP sequence was selected for its high contrast between liver tissue (dark) and blood vessels (bright) [31–33].

Table 1: Overview of key b-SSFP acquisition parameters. ‘Radboud UMC’ refers to the 3T MRI protocol used at Radboud UMC. ‘UTwente’ refers to the 1.5T MRI protocol used at the University of Twente.

Parameter	Radboud UMC	UTwente
Orientation	Transversal	Transversal
Slice thickness	3.0 mm	4.5 mm
Number of slices	40	30
Field of View (FOV)	380 mm × 311 mm	380 mm × 306 mm
Matrix size	320 × 256	320 × 320
Voxel size	1.2 × 1.2 mm ²	1.2 × 1.2 mm ²
Repetition Time (TR)	3.7 ms	4.26 ms
Echo Time (TE)	1.87 ms	2.13 ms
Flip Angle (FA)	41°	60°
Time of acquisition (TA)	0m 19s	0m 20s
Parallel imaging acceleration factor (PE)	2	2

3.2 Manual Data Segmentation

On MRI scans from subjects at Radboud UMC ($n = 23$, male: 12, female: 11, age range: 23–80 years), manual vein segmentation was performed using 3D Slicer (version 5.8.1) [34]. An example of the segmentation is shown in Figure 3. In older subjects, hepatic cysts are not uncommon (see Figure 2). As the b-SSFP sequence renders fluids bright, may appear similar to veins [31, 32]. Therefore, each segmented structure was carefully traced back to the portal vein or vena cava to ensure accuracy.

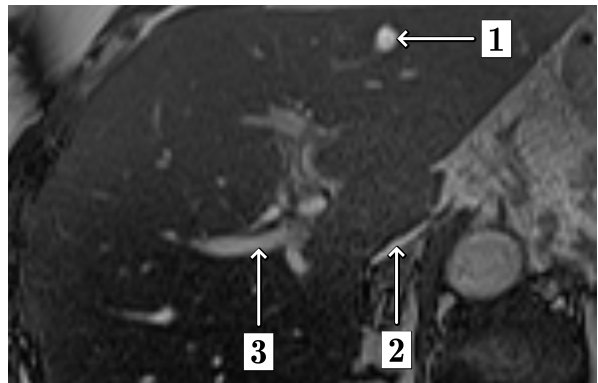


Figure 2: Transverse b-SSFP MRI scan of the liver. Indicated are: **1** – a cyst, **2** – the vena cava, and **3** – the portal vein.

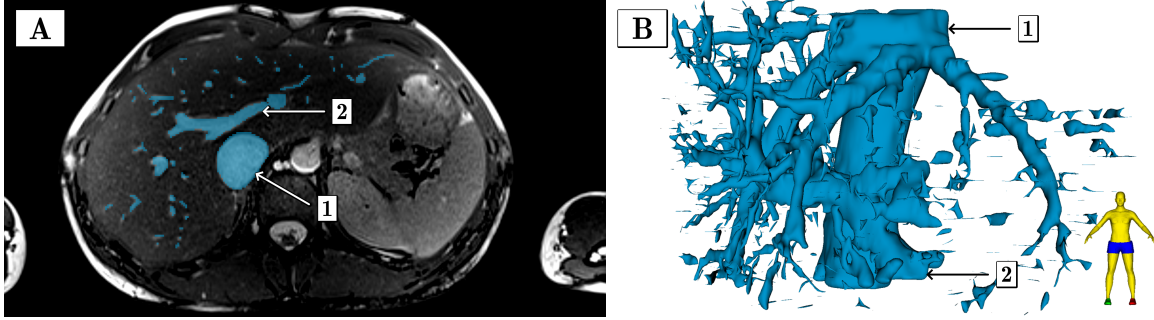


Figure 3: Example of hepatic veins segmentation using 3D Slicer. (A) Transverse b-SSFP MRI scan of the liver, with segmented veins overlaid in blue. (B) 3D rendering of the segmented veins, visualised with smoothing factor 0.3. In both, arrow 1 points to the IVC, arrow 2 to the portal vein.

3.3 AI Model Development

The Radboud UMC MRI data and corresponding segmentations were used as ground truth to train an nnU-Net v2 AI model [30]. A Python script (version 3.12) was written to run nnU-Net v2. During preprocessing, several operations were applied. First, Z-score normalisation was performed without a mask to ensure consistent intensity scaling:

$$Z = \frac{X - \mu}{\sigma}$$

Where Z represents the Z-score, X is the value of a pixel, μ is the mean intensity of the dataset, and σ is the standard deviation of the dataset. Subsequently, all images were resampled to a spacing of [3.0, 1.1875, 1.1875] mm. The model was trained using the *3d_fullres* configuration of nnU-Net. The configuration settings used were automatically optimised by nnU-Net based on the characteristics of the dataset. This configuration employed a network with six layers, where only 2D convolutions were applied in the first layer. The patch size was set to [32, 224, 256], and the batch size was 2. This preprocessing and configuration ensured optimal model training while taking into account the limitations of the available hardware. The loss function used was a *DeepSupervisionWrapper*, which combined the *RobustCrossEntropyLoss()* – a variant of cross-entropy designed to be more stable in the presence of label noise – and the *MemoryEfficientSoftDiceLoss()*, a Dice loss variant optimised for reduced memory consumption. The fold was set to 'all', meaning that the entire dataset from Radboud UMC was used for both training and internal validation. The UTwente dataset served to validate the model on independent data.

3.4 Quantitative Validation

The dataset obtained from the participants was manually segmented. In addition, the trained AI model was used to segment the same dataset. The manual segmentation can then be compared to the AI-generated segmentation by quantifying their volume overlap (see Equation 1), sensitivity (see Equation 2), and specificity (see Equation 3). Due to variability in the number of segmented voxels between segmentations, the Dice score is used to quantify overlap. This analysis enables an evaluation of the model's accuracy.

Let:

$$\begin{aligned} A &= \{x \mid seg_{AI}(x) > 0\}, & A' &= \{x \mid seg_{AI}(x) = 0\} \\ B &= \{x \mid seg_{manual}(x) > 0\}, & B' &= \{x \mid seg_{manual}(x) = 0\} \end{aligned}$$

Then:

$$\text{Dice} = \frac{2 \cdot |A \cap B|}{|A| + |B|} \quad (1) \quad \text{Sensitivity} = \frac{|A \cap B|}{|B|} \quad (2) \quad \text{Specificity} = \frac{|A' \cap B'|}{|B'|} \quad (3)$$

3.5 Qualitative Validation

To identify specific regions where the AI-generated segmentation deviates from the manual segmentation, a 3D reconstruction was performed. For this purpose, three segmentation masks were generated: one containing all voxels overlapping the AI and manual segmentations, one containing all voxels segmented only by the AI model, and one containing voxels present only in the manual segmentation. Each of these masks was assigned a distinct colour to visualise the spatial distribution of discrepancies between the AI and manual segmentations.

As an additional postprocessing step, a binary filtering operation was applied to remove small isolated structures and maintain only clinically relevant regions; namely, the larger hepatic veins and the inferior vena cava. This was performed in 3D Slicer using the 'opening (remove extrusions)' filter, with a kernel size of 3.0 mm.

3.6 In-Vitro Assessment

To investigate the clinical potential of this AI model before and during MRI-guided interventions, a phantom was created for use in an in-vitro study. A computer-generated model of the liver and hepatic veins (as shown in Figure 4) was used [35]. The vessels were printed using fused deposition modeling (FDM) with polyvinyl alcohol (PVA) material. After printing a mold of the liver, the vessels were placed inside the mold, which was then filled with silicone (Ecoflex 00-31 Near Clear, Smooth-On, Macungie, PA). Once the silicone had cured, the phantom was immersed in water to dissolve the PVA as much as possible, resulting in hollow venous structures within the phantom. Subsequently, the phantom — submerged in a water bath to fill the venous structures — was scanned using a 1.5T MRI scanner at UTwente with a 3D b-SSFP sequence (protocol parameters are listed in Table 2). Finally, under MRI guidance, navigation through the hepatic veins was performed using a real-time b-SSFP sequence (parameters can be found in Table 2).

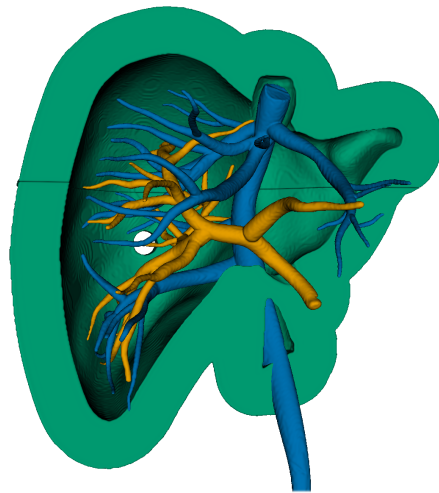


Figure 4: 3D representation of the liver phantom model [35]. Shown are the vena cava (**blue**) and the portal vein (**yellow**) inside one half of the mold (**green**). The front half of the mold is excluded in this view; the filling opening is visible at the back.

Table 2: Overview of the key parameters of the b-SSFP sequences used for phantom imaging.

Parameter	3D b-SSFP	real-time b-SSFP
Orientation	Coronal	Coronal oblique
Slice thickness	1.50 mm	10.0 mm
Number of slices	128	1
Field of view (FOV)	288 mm × 288 mm	224 mm × 224 mm
Matrix size	192 × 192	112 × 112
Voxel size	1.5 × 1.5 mm ²	2.0 × 2.0 mm ²
Repetition time (TR)	3.87 ms	4.1 ms
Echo time (TE)	1.70 ms	2.05 ms
Flip angle (FA)	40°	40°
Temporal resolution	–	172.2 ms

4 Results

4.1 Model Training

The model was trained for a maximum of 250 epochs, starting from an initial learning rate of 0.01 and gradually decreasing to $7 \cdot 10^{-5}$ in the final epoch (Figure 5, bottom). Both the training and the validation loss curves begin to converge gradually after approximately 50 epochs, with continued slow improvement in both training and validation. The best epoch achieved an average pseudo-Dice score of 0.90 on the validation set. The pseudo-Dice score refers to a Dice score calculated (Equation 1) during training on the internal validation data, rather than on a fully independent dataset. The top panel of Figure 5 shows that the model improved over time without signs of overfitting. The small gap between the training and validation loss suggests that the model was able to generalise well. These trends indicate that the model successfully learned to segment hepatic veins and is likely to be applicable to unseen datasets.

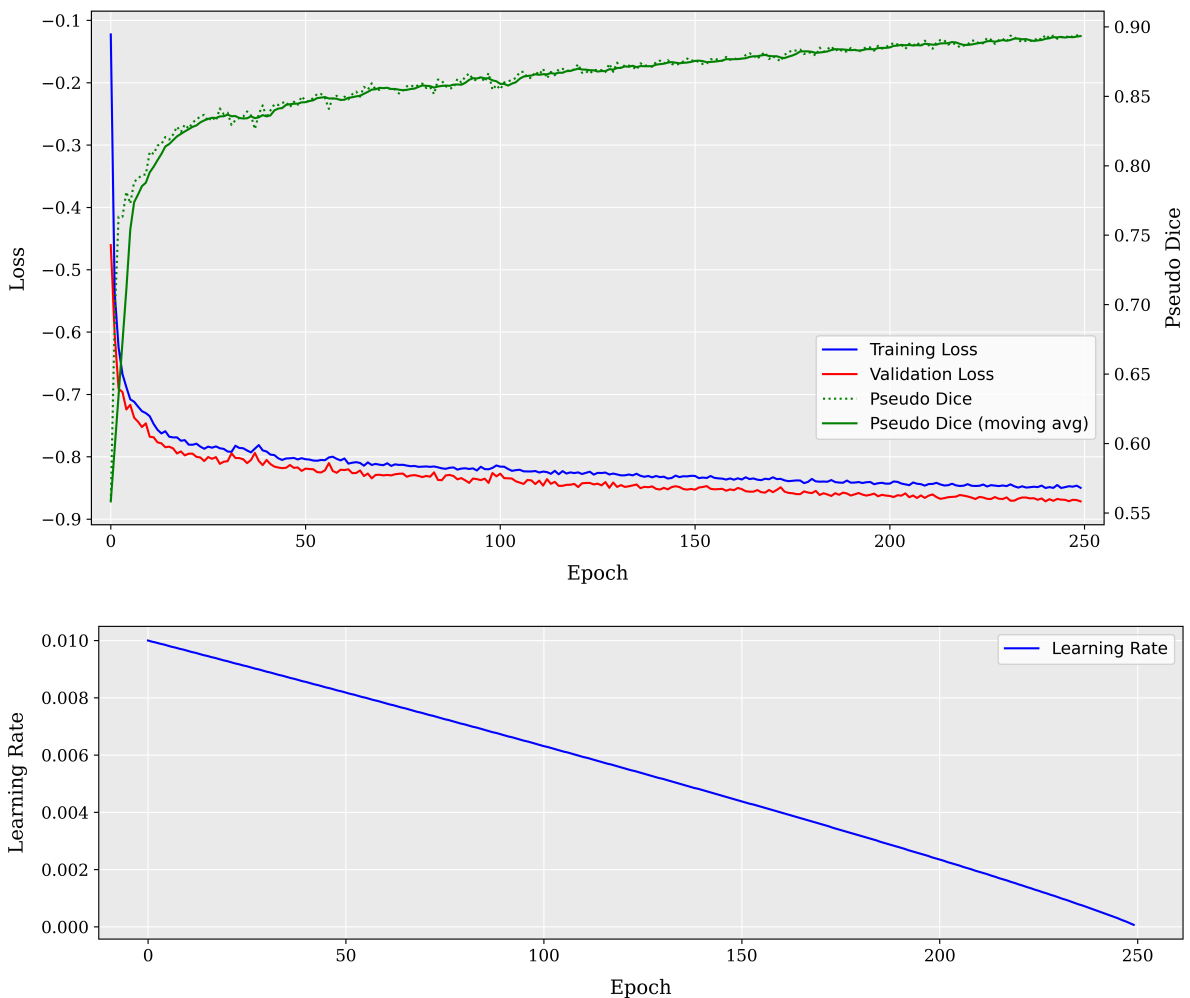


Figure 5: Learning curves over 250 epochs. **Top:** Training loss (blue) and validation loss (red) plotted against the number of epochs, alongside the pseudo-Dice score (dotted green) and its moving average (solid green) on the validation set. The pseudo-Dice score increases consistently progression throughout training, reaching approximately 0.90 in the final epoch. No signs of overfitting are observed. **Bottom:** The learning rate decreases during training, starting at approximately 0.01 and ending at around $7 \cdot 10^{-5}$.

4.2 Model Validation

A quantitative analysis was performed by calculating the Dice score, sensitivity, and specificity. The manual segmentation served as the ground truth against which the AI-generated segmentation was compared. The results are presented in Table 3. For participant 1, the model achieved a Dice score of 0.86, a sensitivity of approximately 0.84, and a specificity of approximately 1.00. These results indicate that the model provides a close approximation of the ground truth segmentation. However, the sensitivity suggests that the AI segmentation contains a considerable number of false negative voxels. In contrast, the high specificity indicates that the AI model produces very few false positives.

Table 3: Quantitative comparison between AI-generated and manual segmentations of the hepatic veins across four participants (male: 1, female: 3). The Dice score (calculated using Equation 1), sensitivity (Equation 2), and specificity (Equation 3) were computed for each individual participant, and the average scores are also reported.

Participant	Dice-score	Sensitivity	Specificity
1	0.86	0.84	1.00
2	0.88	0.86	1.00
3	0.87	0.83	1.00
4	0.89	0.87	1.00
Average:	0.88 ± 0.01	0.85 ± 0.02	1.00 ± 0.00

In addition to the quantitative analysis, a qualitative assessment was performed to provide insight into the cause of the discrepancies between manual and AI segmentations. As shown in Figure 6, the majority of the segmented volume consists of overlapping regions (depicted in green), indicating that the AI model largely identifies the same voxels as the manual segmentation. Deviations are visible in yellow (voxels segmented only in the manual annotation) and blue (voxels segmented only by the AI). Notably, these differences are predominantly located in small peripheral vascular structures.

Furthermore, it was observed that the regions missed by the AI model often include fine vessel branches that serve as connectors between smaller and larger venous structures. In addition, the manual segmentation tends to outline the vascular lumen slightly larger than the AI segmentation, which may cause the tendency of the AI model to under-segment in regions with low image contrast.

In participant 1 and participant 4, the AI model failed to segment a portion of the portal vein on the caudal side. In participant 4, it was also noted that an entire branch of the right hepatic vein, as well as a branch of the left hepatic vein, were not segmented by the AI.

4.3 Postprocessing

The three-dimensional (3D) reconstructions are shown in Figure 7. This 3D rendering resulted from the 'opening (remove extrusions)' operation, performed without applying a smoothing factor, illustrating the staircasing effect due to the low resolution in the longitudinal direction. It can also be observed that small vascular structures were removed as a result of the post-processing step, and that the manual segmentation yields an anatomically very similar reconstruction.

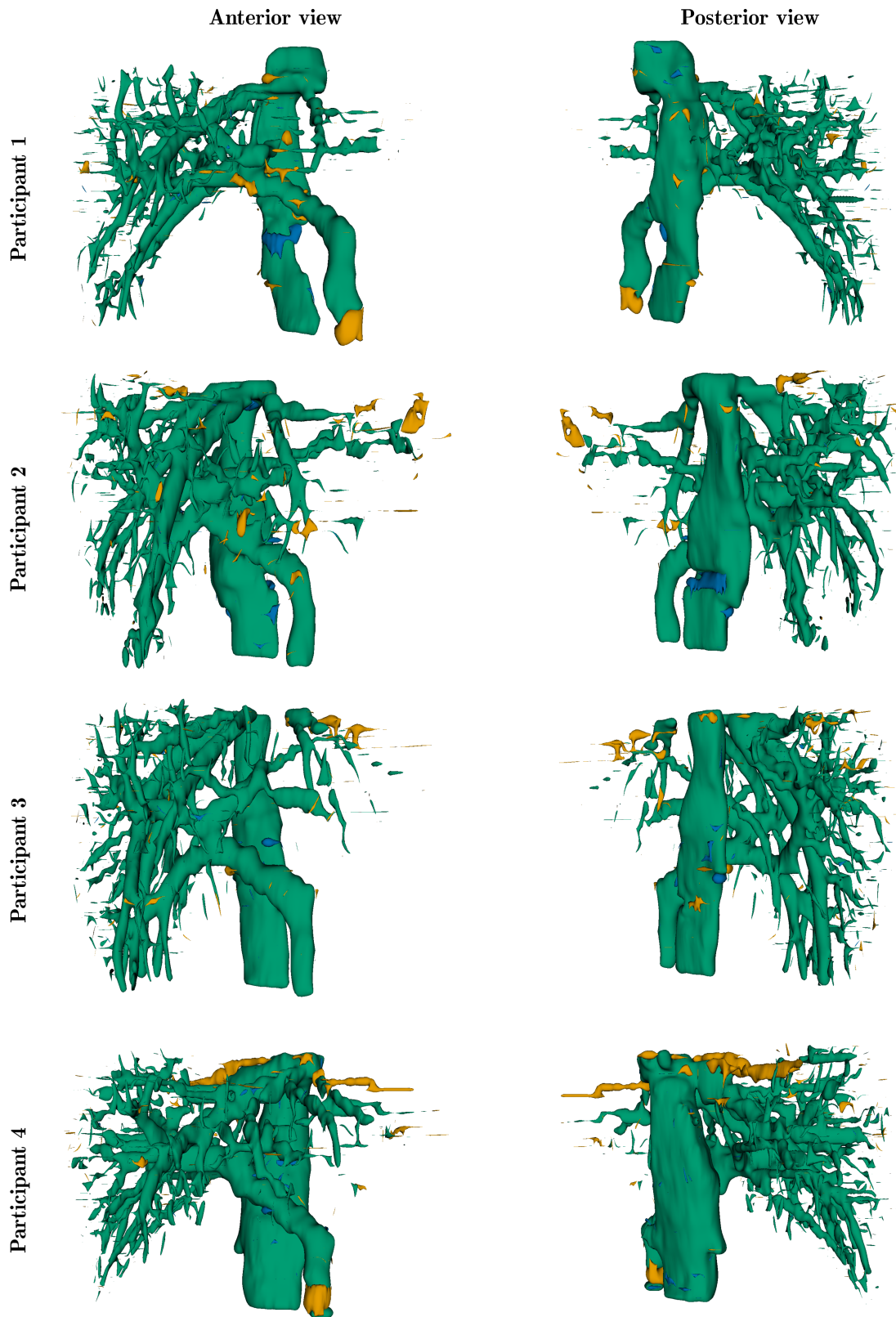


Figure 6: 3D visualisation (smoothing factor 0.3) comparing manual and AI-generated segmentations of hepatic veins. Overlapping regions between the manual and AI segmentations are shown in **green**, manual-only segmented regions in **yellow**, and AI-only segmented regions in **blue**. Each row represents a different participant (from top to bottom: participants 1-4), with anterior and posterior views shown on the left and right, respectively.

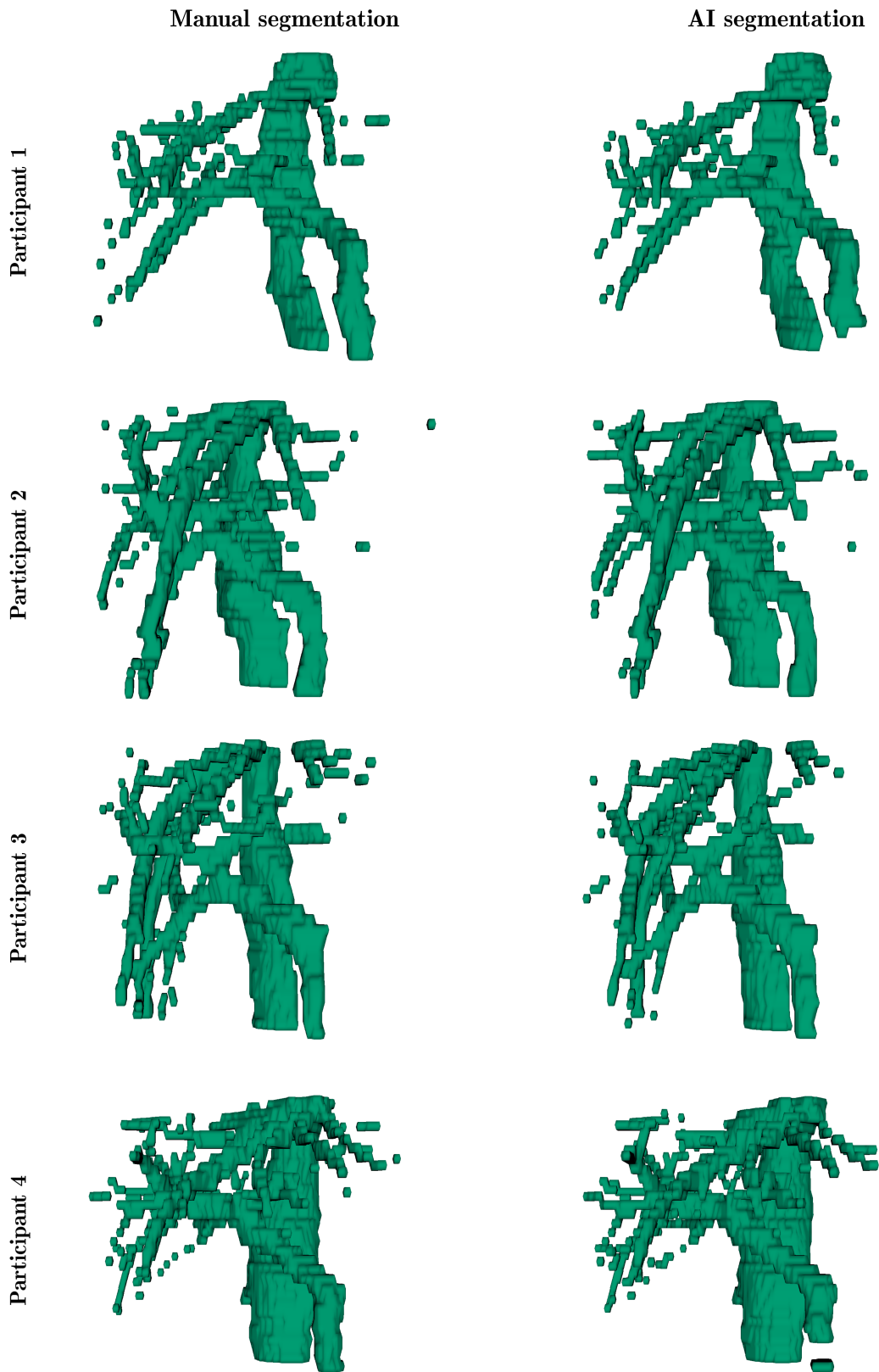


Figure 7: 3D visualisation without smoothing factor, with postprocessing filter applied, resulting in the removal of small vascular structures. All views are shown from an anterior perspective. Each row represents a different participant (from top to bottom: participants 1-4), with the manual segmentation shown on the left and the AI-generated segmentation on the right.

4.4 Phantom Intervention

First, a segmentation was created on the 3D b-SSFP scan using the 'grow from seeds' module in 3D Slicer. The 3D reconstruction of this segmentation is shown in Figure 8. Subsequently, an MRI-compatible catheter was advanced through the inferior vena cava under MRI guidance. This procedure was recorded using the real-time b-SSFP sequence. Through post-processing in 3D Slicer, the 3D segmentation could be overlaid onto the real-time 2D imaging (as shown in Figure 9).

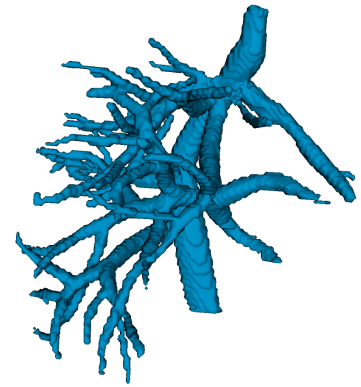


Figure 8: 3D reconstruction of the segmented venous structures in the liver phantom, based on the 3D b-SSFP sequence.

The figure displays a series of static frames, but using specialised software (in this case 3D Slicer), this 3D overlay can be interactively rotated and translated in all six degrees of freedom (namely, translation and rotation along the three orthogonal axes). The frames illustrate that the catheter's position can be continuously tracked, and the 3D overlay provides the operator with a clear visual reference of the catheter's location in three-dimensional space. This visualisation also aids in identifying which vascular branch should be targeted during navigation.

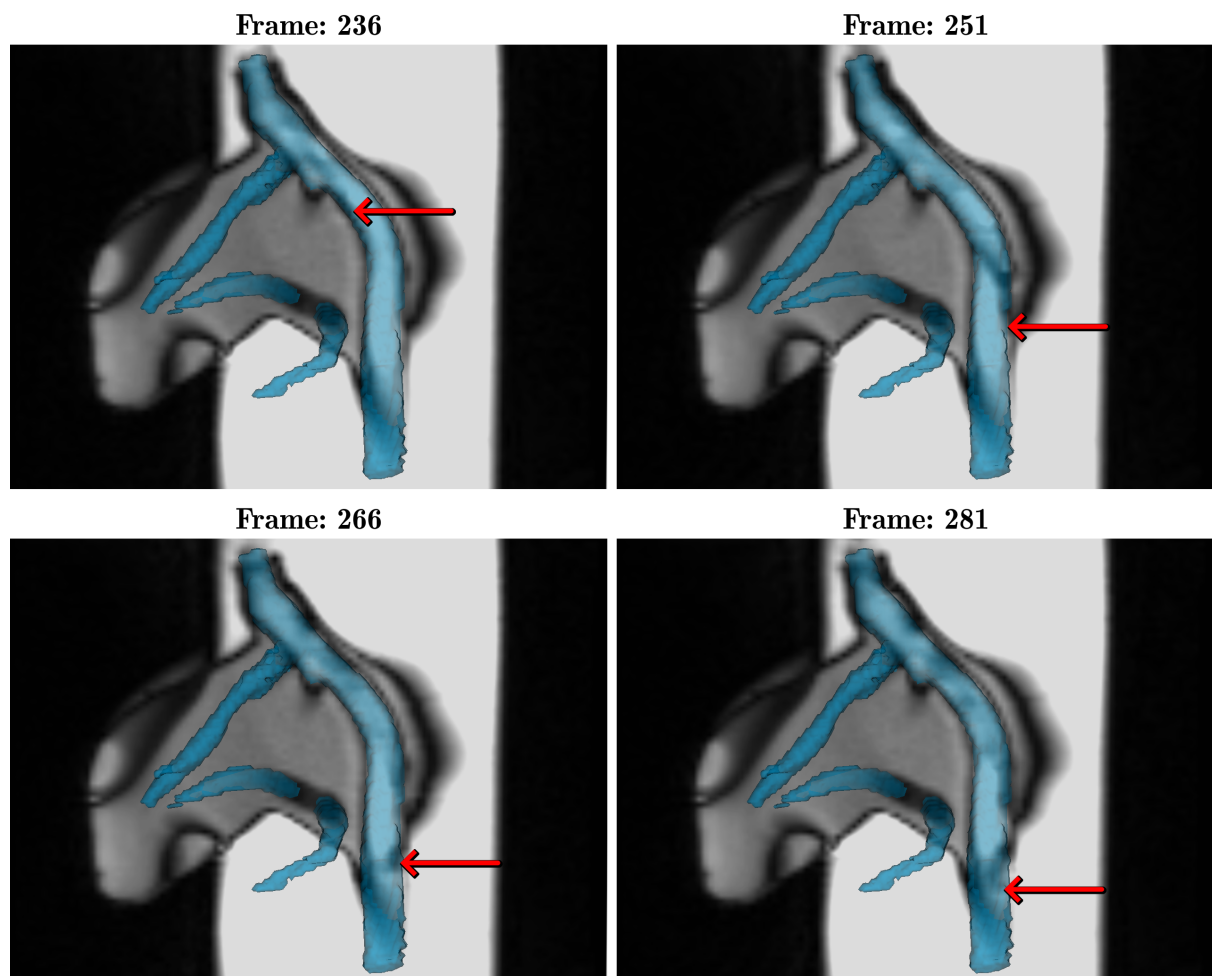


Figure 9: Four frames from the MRI-guided real-time b-SSFP acquisition with an overlaid 3D segmentation. Between frame 236 and frame 281, the catheter was advanced through the inferior vena cava. The catheter tip is indicated by red arrows.

5 Discussion

In this study, the feasibility of accurately segmenting the hepatic veins on non-contrast MRI using an AI model was investigated. A 3D full-resolution nnU-Net version 2 framework was used and trained on 23 manually segmented b-SSFP MRI scans. The model achieved an average pseudo-Dice score of 0.90 on an internal validation set. Validation on an independent dataset, which was not used during training and consisted of four manually segmented MRI scans, yielded an average Dice score of 0.88 ± 0.01 , an average sensitivity of 0.85 ± 0.02 , and an average specificity of 1.00 ± 0.00 . These scores are significantly higher than those reported by Zbinden et al., who also employed a nnU-Net framework, but for the separate segmentation of the liver, portal vein, and hepatic veins on a T1 volumetric interpolated breath-hold examination (VIBE) Dixon sequence [28]. The AI model in their study achieved a Dice score of 0.643 ± 0.09 for the portal vein and 0.532 ± 0.12 for the hepatic veins. The fact that Zbinden et al. trained the model to segment the portal vein and hepatic veins separately may have introduced an additional level of difficulty, potentially contributing to the lower Dice scores.

Visual analysis indicated that the majority of the segmented venous lumen corresponded well to the ground truth. Discrepancies were mainly observed in small peripheral vessels and along the outer edge of the lumen. Furthermore, Figure 7 demonstrates that filtering out small vascular structures results in a clear 3D reconstruction of the major vessels relevant for endovascular interventions. One can appreciate that the AI segmentations visually correspond to the manual segmentations in terms of anatomical branching and spatial orientation. However, it should be noted that the vascular structures exhibit low spatial resolution in the longitudinal direction, which is due to the relatively large slice thickness (4.5 mm). Improvements in this aspect could enhance segmentation clarity. Despite the limited size of both the training and validation datasets, the model demonstrated successful generalisation to previously unseen data, supported by the learning curves showing no signs of overfitting (as was shown in Figure 5).

Both qualitative and quantitative analyses support these findings: the AI model is capable of segmenting the main structures of the hepatic and portal veins. Although small peripheral venous branches were occasionally missed, this is unlikely to be clinically significant when these small vessels are filtered out. These results suggest that the AI model holds potential for generating vascular maps from non-contrast MRI.

5.1 Clinical Implications

Research by Zhu et al. has demonstrated that 3D reconstruction of the cerebral veins during catheterisation, serving as procedural roadmap, is of critical importance [36]. The 3D projection can be freely rotated by the interventionalist, allowing for enhanced visualisation of anatomical structures. This facilitates catheter navigation and optimises placement accuracy, thereby reducing the risk of complications due to inadvertent navigation into an incorrect lumen. However, this method relies on real-time intraoperative imaging using ionising radiation, which poses a potential risk to both patients and medical staff. In contrast, this study focuses on the generation of preoperative imaging using non-invasive and non-ionising methods.

The importance of 3D visualisation in endovascular interventions is further supported by Kishore et al., who employed contrast-enhanced 3D magnetic resonance venography (MRV) [37]. Their study demonstrated a significant increase in clinician confidence regarding the anatomy of the cortical veins, as measured by a 3-point Likert scale (1 = low confidence; 3 = high confidence). Scores improved from 1.9 to 2.9 ($p = 0.001$), highlighting the clinical value of 3D venous imaging. When extrapolating these findings from cerebral to hepatic endovascular interventions, the AI model proposed in this study has the potential to aid the interventionalist

with a non-toxic preoperative roadmap, despite the lack of real-time imaging.

While this study primarily aimed to develop an AI model capable of generating preoperative venous segmentation, an initial phantom experiment was conducted to explore its potential use during interventions. This initial study demonstrated that real-time MRI acquisition – comparable to conventional fluoroscopy – combined with a post-processed 3D overlay, can accurately depict the catheter’s position within the venous system. These findings suggest that AI-based 3D segmentation may not only support preoperative planning, but also assist intraoperative navigation by providing spatial context during catheter navigation.

Moreover, the findings of this study indicate that the combination of a b-SSFP sequence with the proposed AI model eliminates the need for contrast agents altogether. Prior research has identified potential toxic side effects of GBCAs in patients [20–22]. Recent advances have demonstrated that the integration of AI can significantly reduce the required dose of GBCAs [23–26]. In contrast, using AI for segmentation effectively removes the risks associated with GBCA administration, such as anaphylaxis and nephrotoxicity, thereby enabling a safer and less invasive imaging approach for patients.

5.2 Study Limitations

There are several important limitations to keep in mind when analysing the results of this study. The ground truth segmentations used to train the model were created by a researcher, not by a trained radiology technician or interventional radiologist. Although care was taken to accurately segment the veins and exclude surrounding tissues, the lack of clinical experience might have introduced some errors. These potential inaccuracies in the training labels could impact the model’s performance, as deep learning models depend heavily on precise annotations. Besides, the training dataset included only 23 scans, which means that any single annotation error could have a relatively large impact on the final model performance compared to a situation in which a larger dataset had been used.

Another limitation to consider is the imaging parameters of the validation dataset. These scans were taken using a 1.5 Tesla MRI with a slice thickness of 4.5 mm, whereas the training data used a thinner slice of 3.0 mm. The thicker slices and lower magnetic field strength resulted in reduced spatial resolution, particularly in the z-direction (cranio-caudal axis). This directly affected the visibility of small vascular structures, especially veins running predominantly in the transverse plane. As a consequence such vessels were sometimes missed or only partially segmented. This could lead to 3D visualisations of the segmentation appearing incomplete, with some vessels disconnected. For pre-operative roadmapping, it is particularly important that vascular connectivity is accurately represented in order to plan the catheter route effectively.

Respiratory motion artifacts were observed in several scans from the Radboud UMC dataset, particularly in older participants. These artifacts may have caused anatomical structures to be misaligned, which can result in the AI model being trained on distorted or inaccurate images. As a result, this may have negatively impacted the overall performance of the model.

Finally, the validation dataset only included young, healthy volunteers without hepatic cysts. Although the training data did contain scans with hepatic cysts and the AI model was trained to avoid segmenting these, this cannot be verified using the current validation set. Since hepatic cysts are more common in older individuals and appear similarly bright as veins on b-SSFP sequences, it remains uncertain how the model would behave when segmenting data from a patient with hepatic cysts. The model’s ability to differentiate between cysts and actual vascular structures has therefore not been conclusively validated.

5.3 Recommendation

As previously demonstrated, the proposed AI model is capable of accurately segmenting the venous structures in the liver, the model could be further improved by enabling the separate segmentation of the hepatic veins and the portal vein. Currently, all venous structures are segmented together, which can lead to confusion for the interventionalist, especially in cases such as BCS, where only inferior vena cava and hepatic veins are clinically relevant. In contrast, during catheterisation procedures for portal vein thrombosis [38], segmentation of the portal vein becomes clinically essential. Therefore, it would be an advantage if the AI model could distinguish between different venous structures, allowing the clinician to selectively visualise the vessels of interest.

Zbinden et al. have demonstrated with their AI model that there is still room for improvement in terms of separate venous segmentation [28]. Now that AI has proven to be capable of accurate venous segmentation and its clinical importance has been established, the model could be further developed and integrated into hospital workflows. This would allow the model to be continuously trained on a larger and more representative dataset, including variations such as cysts, specific anatomical abnormalities, or imaging artifacts.

The initial phantom experiment suggests that MRI-guided endovascular interventions may become feasible in the future. However, several technical limitations were observed. Most notably, catheter visibility on the b-SSFP sequence was limited when the catheter was stationary, but further enhancement is necessary to make static positioning clearly noticeable. One potential solution could be the use of gadolinium-coated catheters or incorporating materials in the catheter tip that provide better contrast on b-SSFP imaging. Alternatively, catheter tip tracking could be achieved using small embedded coils, with spatial location rendered in the 3D reconstruction via software animation. However, this approach may increase catheter diameter, which could be clinically undesirable. Additionally, the current 2D real-time b-SSFP sequence presents a limitation for MRI-guided interventions, as the catheter is no longer visible when moving out of the imaging plane. Improved 3D real-time imaging sequences or spatial tracking may offer the solution to this constraint.

6 Conclusion

This study demonstrated that a deep learning convolutional neural network, based on the nnU-Net v2 framework, is capable of accurately segmenting hepatic venous structures on non-contrast MRI using a b-SSFP sequence. The AI model achieved a high Dice score of 0.90, indicating strong agreement with manual annotations, even when validated on an independent dataset (Dice score: 0.88 ± 0.01). With a sensitivity of 0.85, the AI model still exhibits some false-negative voxels, primarily in regions containing small peripheral vessels with lower image contrast. However, the majority of these vessels are not relevant during an intervention and are removed during post-processing to improve the 3D visualisation and focus on the clinically relevant larger venous structures during navigation. Although in certain specific cases involving stenting the preservation of small vascular structures may be important, these could potentially be included in a separate segmentation channel.

Learning curves and performance on the external dataset suggest that the AI model generalises well to new subjects, confirming its robustness. These findings support the use of AI-based segmentations for generating patient-specific 3D reconstructions in the preoperative phase. Such reconstructions provide interventional radiologists with an enhanced understanding of spatial anatomy, potentially leading to more accurate catheter navigation and fewer complications.

If the use of MRI-guided interventions becomes more feasible in the future, real-time intraoperative segmentation by AI may further support these procedures. As a result, the need for ionising radiation, iodine-based contrast media, or gadolinium contrast agents could be entirely eliminated.

In summary, this study shows that accurate liver vein segmentation without contrast agents is both feasible and clinically relevant. With further validation and integration into clinical workflows, this technology could contribute to safer and more accessible endovascular interventions for Budd-Chiari Syndrome and other related vascular conditions.

7 Acknowledgments

I would like to thank my supervisor, Dr. Ir. Wyger Brink, for guiding this research, providing valuable feedback, and sharing his knowledge, from which I have learned a great deal. I have enjoyed his enthusiastic curiosity, which ultimately also led to the realisation of the phantom intervention.

I also wish to thank the other members of my graduation committee - MSc Eva Ilija and Ir. Jan van der Hoek - for their support during this project. I am especially grateful to Anne van den Brekel from Radboud UMC for providing access to the MRI data.

Additionally, I would like to thank all the participants at Radboud UMC and the University of Twente for undergoing an MRI scan and making their data available for this study.

Finally, I would like to thank my parents for their support throughout my bachelor. Whether it was for relaxation, someone to talk to, feedback on my writing, or in-depth medical explanations – I could always count on them.

References

- [1] H. Ferral, G. Behrens, J. Lopera, H. Ferral, G. Behrens, and J. Lopera. “Budd-Chiari Syndrome”. In: *Am. J. Roentgenol.* (Nov. 2012). DOI: 10.2214/AJR.12.9098.
- [2] D.-C. Valla. “Primary Budd-Chiari syndrome”. In: *J. Hepatol.* 50.1 (Jan. 2009), pp. 195–203. DOI: 10.1016/j.jhep.2008.10.007.
- [3] L. D. DeLeve, D.-C. Valla, and G. Garcia-Tsao. “Vascular Disorders of the Liver”. In: *Hepatology (Baltimore, Md.)* 49.5 (May 2009), p. 1729. DOI: 10.1002/hep.22772.
- [4] P. Gruselle, P. Ooghe, P. Cauchie, and G. Van der Cruyssen. “Severe thrombophilic diathesis starting with hepatic vein thrombosis (BUDD-CHIARI syndrome) in a family with a new Protein S gene mutation”. In: *Acta Gastroenterol. Belg.* 69.1 (Jan. 2006), pp. 20–24.
- [5] *Hepatic Veins*. [Online; accessed 24. May 2025]. May 2025. URL: <https://my.clevelandclinic.org/health/body/hepatic-veins>.
- [6] M. Aydinli and Y. Bayraktar. “Budd-Chiari syndrome: Etiology, pathogenesis and diagnosis”. In: *World Journal of Gastroenterology : WJG* 13.19 (May 2007), p. 2693. DOI: 10.3748/wjg.v13.i19.2693.
- [7] R. M. Goel, E. L. Johnston, K. V. Patel, and T. Wong. “Budd-Chiari syndrome: investigation, treatment and outcomes”. In: *Postgrad. Med. J.* 91.1082 (Dec. 2015), pp. 692–697. DOI: 10.1136/postgradmedj-2015-133402.
- [8] N. Jagtap, M. Sharma, J. Singh, M. Tandan, P. N. Rao, R. Gupta, S. Lakhtakia, M. Ramchandani, H. Shah, T. Mahesh Kumar, S. Darishetty, G. V. Rao, and D. N. Reddy. “Budd-Chiari syndrome: outcomes of endovascular intervention—A single-center experience”. In: *Indian J. Gastroenterol.* 36.3 (May 2017), pp. 209–216. DOI: 10.1007/s12664-017-0760-6.
- [9] A. Mukund, K. Mittal, A. Mondal, and S. K. Sarin. “Anatomic Recanalization of Hepatic Vein and Inferior Vena Cava versus Direct Intrahepatic Portosystemic Shunt Creation in Budd-Chiari Syndrome: Overall Outcome and Midterm Transplant-Free Survival”. In: *J. Vasc. Interv. Radiol.* 29.6 (June 2018), pp. 790–799. DOI: 10.1016/j.jvir.2018.01.781.
- [10] W. Zhang, Q.-Z. Wang, X.-W. Chen, H.-S. Zhong, X.-T. Zhang, X.-D. Chen, and K. Xu. “Budd-Chiari syndrome in China: A 30-year retrospective study on survival from a single center”. In: *World J. Gastroenterol.* 24.10 (Mar. 2018), p. 1134. DOI: 10.3748/wjg.v24.i10.1134.
- [11] A. Sharma, S. N. Keshava, A. Eapen, E. Elias, and C. E. Eapen. “An Update on the Management of Budd-Chiari Syndrome”. In: *Dig. Dis. Sci.* 66.6 (June 2021), pp. 1780–1790. DOI: 10.1007/s10620-020-06485-y.
- [12] K. Rathod, H. Deshmukh, A. Shukla, B. Popat, A. Pandey, A. Gupte, D. K. Gupta, and S. J. Bhatia. “Endovascular treatment of Budd-Chiari syndrome: Single center experience”. In: *J. Gastroenterol. Hepatol.* 32.1 (Jan. 2017), pp. 237–243. DOI: 10.1111/jgh.13456.
- [13] A. Oropallo and C. A. Andersen. “Venous Stenting”. In: *StatPearls [Internet]*. StatPearls Publishing, Aug. 2023. URL: <https://www.ncbi.nlm.nih.gov/books/NBK574515>.
- [14] P. Chinnadurai and J. Bismuth. “Intraoperative Imaging and Image Fusion for Venous Interventions”. In: *Methodist DeBakey Cardiovascular Journal* 14.3 (July 2018), p. 200. DOI: 10.14797/mdcj-14-3-200.
- [15] W. Rühm, D. Laurier, and R. Wakeford. “Cancer risk following low doses of ionising radiation – Current epidemiological evidence and implications for radiological protection”. In: *Mutation Research/Genetic Toxicology and Environmental Mutagenesis* 873 (Jan. 2022), p. 503436. DOI: 10.1016/j.mrgentox.2021.503436.

- [16] Z. Drew. “Radiation dose considerations in CT fluoroscopy”. In: *Radiopaedia* (Nov. 2020). DOI: 10.53347/rID-62862.
- [17] B. Di Muzio. “Iodinated contrast media adverse reactions”. In: *Radiopaedia* (Oct. 2024). DOI: 10.53347/rID-42772.
- [18] L. J. Scott. “Gadobutrol: A Review in Contrast-Enhanced MRI and MRA”. In: *Clin. Drug Invest.* 38.8 (Aug. 2018), pp. 773–784. DOI: 10.1007/s40261-018-0674-9.
- [19] P. L. Choyke, P. Yim, H. Marcos, V. B. Ho, R. Mullick, and R. M. Summers. “Hepatic MR angiography: a multiobserver comparison of visualization methods”. In: *AJR Am. J. Roentgenol.* 176.2 (Feb. 2001), pp. 465–470. DOI: 10.2214/ajr.176.2.1760465.
- [20] D. W. Raisch, V. Garg, R. Arabyat, X. Shen, B. J. Edwards, F. H. Miller, J. M. McKoy, B. Nardone, and D. P. West. “Anaphylaxis associated with gadolinium-based contrast agents: data from the Food and Drug Administration’s Adverse Event Reporting System and review of case reports in the literature”. In: *Expert Opin. Drug Saf.* 13.1 (Jan. 2014), pp. 15–23. DOI: 10.1517/14740338.2013.832752.
- [21] S. Lange, W. Mędrzycka-Dąbrowska, K. Zorena, S. Dąbrowski, D. Ślęzak, A. Malecka-Dubiela, and P. Rutkowski. “Nephrogenic Systemic Fibrosis as a Complication after Gadolinium-Containing Contrast Agents: A Rapid Review”. In: *Int. J. Environ. Res. Public Health* 18.6 (Mar. 2021), p. 3000. DOI: 10.3390/ijerph18063000.
- [22] L. Blomqvist, G. F. Nordberg, V. M. Nurchi, and J. O. Aaseth. “Gadolinium in Medical Imaging—Usefulness, Toxic Reactions and Possible Countermeasures—A Review”. In: *Biomolecules* 12.6 (May 2022), p. 742. DOI: 10.3390/biom12060742.
- [23] C. A. Mallio, A. Radbruch, K. Deike-Hofmann, A. J. van der Molen, I. A. Dekkers, G. Zaharchuk, P. M. Parizel, B. B. Zobel, and C. C. Quattrocchi. “Artificial Intelligence to Reduce or Eliminate the Need for Gadolinium-Based Contrast Agents in Brain and Cardiac MRI: A Literature Review”. In: *Invest. Radiol.* 58.10 (Oct. 2023), pp. 746–753. DOI: 10.1097/RLI.0000000000000983.
- [24] R. Haase, T. Pinetz, Z. Bendella, E. Kobler, D. Paech, W. Block, A. Effland, A. Radbruch, and K. Deike-Hofmann. “Reduction of Gadolinium-Based Contrast Agents in MRI Using Convolutional Neural Networks and Different Input Protocols: Limited Interchangeability of Synthesized Sequences With Original Full-Dose Images Despite Excellent Quantitative Performance”. In: *Invest. Radiol.* 58.6 (June 2023), pp. 420–430. DOI: 10.1097/RLI.0000000000000955.
- [25] R. Haase, T. Pinetz, E. Kobler, D. Paech, A. Effland, A. Radbruch, and K. Deike-Hofmann. “Artificial Contrast: Deep Learning for Reducing Gadolinium-Based Contrast Agents in Neuroradiology”. In: *Invest. Radiol.* 58.8 (Aug. 2023), pp. 539–547. DOI: 10.1097/RLI.0000000000000963.
- [26] B. Tsui, E. Calabrese, G. Zaharchuk, and A. M. Rauschecker. “Reducing Gadolinium Contrast With Artificial Intelligence”. In: *J. Magn. Reson. Imaging* 60.3 (Sept. 2024), pp. 848–859. DOI: 10.1002/jmri.29095.
- [27] S. O. Haarbye, M. B. Nielsen, A. E. Hansen, and C. A. Lauridsen. “Four-Dimensional Flow MRI of Abdominal Veins: A Systematic Review”. In: *Diagnostics* 11.5 (Apr. 2021), p. 767. DOI: 10.3390/diagnostics11050767.
- [28] L. Zbinden, D. Catucci, Y. Suter, A. Berzigotti, L. Ebner, A. Christe, V. C. Obmann, R. Sznitman, and A. T. Huber. “Convolutional neural network for automated segmentation of the liver and its vessels on non-contrast T1 vibe Dixon acquisitions”. In: *Sci. Rep.* 12.22059 (Dec. 2022), pp. 1–11. DOI: 10.1038/s41598-022-26328-2.

- [29] S.-H. Park, P. K. Han, and S. H. Choi. “Physiological and Functional Magnetic Resonance Imaging Using Balanced Steady-state Free Precession”. In: *Korean J. Radiol.* 16.3 (May 2015), p. 550. DOI: 10.3348/kjr.2015.16.3.550.
- [30] F. Isensee, P. F. Jaeger, S. A. A. Kohl, J. Petersen, and K. H. Maier-Hein. “nnU-Net: a self-configuring method for deep learning-based biomedical image segmentation”. In: *Nature methods* 18.2 (Feb. 2021), pp. 203–211. DOI: 10.1038/s41592-020-01008-z.
- [31] *TrueFISP MRI | FIESTA MRI | balanced SARGE | BASG | STERF | SSFP physics and image appearance*. [Online; accessed 28. May 2025]. Oct. 2023. URL: <https://mrimaster.com/characterise-image-trufi>.
- [32] Y. Weerakkody. “TRUFI sequence”. In: *Radiopaedia* (Aug. 2023). DOI: 10.53347/rID-174030.
- [33] A. Er, N. Uzunlulu, T. Guzelbey, S. Yavuz, A. Kiyak, and A. Kayhan. “The nutcracker syndrome: The usefulness of different MRI sequences for diagnosis and follow-up”. In: *Clin. Imaging* 55 (May 2019), pp. 144–147. DOI: 10.1016/j.clinimag.2019.02.003.
- [34] A. Fedorov, R. Beichel, J. Kalpathy-Cramer, J. Finet, J.-C. Fillion-Robin, S. Pujol, C. Bauer, D. Jennings, F. M. Fennessy, M. Sonka, J. Buatti, S. R. Aylward, J. V. Miller, S. Pieper, and R. Kikinis. “3D Slicer as an Image Computing Platform for the Quantitative Imaging Network”. In: *Magnetic Resonance Imaging* 30.9 (Nov. 2012), pp. 1323–1341. DOI: 10.1016/j.mri.2012.05.001.
- [35] H. Ruitenbeek. *Development of a multimodal anthropomorphic liver phantom for the improvement of navigated tumour treatment*. Dec. 2019. URL: <http://essay.utwente.nl/81528/>.
- [36] F. Zhu, L. Liao, S. Bracard, O. Harsan, L. L. De Medeiros, A.-L. Derelle, M. Braun, B. Gory, and R. Anxionnat. “3D digital subtracted angiography venous roadmapping for endovascular management of dural venous stenosis”. In: *Interventional Neuroradiology* (Feb. 2024), p. 15910199241236323. DOI: 10.1177/15910199241236323.
- [37] V. Kishore, S. H. Sundararajan, R. Doustaly, M. Michael, D. Xuan, T. Link, B. Rapoport, and A. Patsalides. “Magnetic resonance venography for 3-dimensional live guidance during venous sinus stenting”. In: *CVIR Endovasc.* 3.1 (Dec. 2020), pp. 1–6. DOI: 10.1186/s42155-020-00158-7.
- [38] C. Ju, X. Li, S. Gadani, B. Kapoor, and S. Partovi. “Portal Vein Thrombosis: Diagnosis and Endovascular Management”. In: *RoFo Fortschr. Geb. Rontgenstr. Nuklearmed.* 194.2 (Feb. 2022), pp. 169–180. DOI: 10.1055/a-1642-0990.